EES Catalysis

ROYAL SOCIETY OF CHEMISTRY

PAPER

View Article Online
View Journal | View Issue

Cite this: *EES Catal.*, 2025, **3**, 119

Carbon incorporated isotype heterojunction of poly(heptazine imide) for efficient visible light photocatalytic hydrogen evolution†

Ping Niu, ‡*[a] Haoqing Zhang,‡[a] Jian Zeng,‡[a] Tianjian Hu,[a] Meixue Zhang,[a] Chengyao Xie,[a] Boyin Zhai,[b] Jérémy Odent, [c] Shulan Wang [b] and Li Li*[a]

Received 18th July 2024,
Accepted 6th November 2024

DOI: 10.1039/d4ey00145a

rsc.li/eescatalysis

Clean hydrogen production using renewable solar energy is an important aspect in the development of a sustainable society. The premise of developing highly efficient photocatalysts for hydrogen production relies on achieving smooth charge carrier kinetics with efficient visible light absorption. Constructing isotype heterojunctions with structural or compositional similarity can enhance charge carrier separation at the interface, leading to improved utilization of light energy. However, this approach is often constrained by the availability as well as intrinsic properties of monomers. Herein, carbon facilitated *in situ* fabrication of an isotype heterojunction based on a poly(heptazine imide) (PHI) structure with high crystallinity and extended π-conjugation was proposed by calcinating carbon-modified melon in the "semi-liquid" NaCl/KCl salt. The heterojunction effect induced by the visible light responsive Na–PHI and K–PHI, as well as the strong charge coupling between heptazine and carbon ring in the covalent interface forms multi-directional built-in electric field and effectively promotes the separation of charge carriers. Together with the visible light absorption extension by simultaneous carbon ring decoration, C@Na–PHI/K–PHI shows superior photocatalytic hydrogen evolution activities under visible light irradiation and the apparent quantum efficiencies reach 29.3% and 3% under 420 and 550 nm, respectively. This study pioneers the idea and provides a useful reference for the design of PHI isotype heterojunctions for the effective utilization of solar energy.

Broader context

Heterojunctions with build-in electric fields have shown great advantages in photocatalytic reactions by influencing the behavior of charge carriers. However, simultaneously promoting smooth charge transfer kinetics and extending visible light absorption for high light converting efficiencies remain a challenge. In this work, by incorporating carbon rings into the melon framework and applying ionothermal treatment using the "semi-liquid" NaCl/KCl salt, a carbon-modified isotype heterojunction based on poly(heptazine imide) (PHI) structure was constructed (C@Na–PHI/K–PHI). The high crystallinity induced efficient charge carrier transfer in PHI, while the heterojunction effect driven by Na–PHI and K–PHI as well as the strong charge coupling between heptazine and carbon ring in the covalent interface, promoted effective utilization of charge carriers. Together with the visible light absorption extension by simultaneous carbon ring decoration, C@Na–PHI/K–PHI shows superior photocatalytic hydrogen evolution activities under visible light irradiation. This study pioneers the idea and provides useful reference for the design and construction of highly efficient photocatalysts for clean hydrogen production.

1. Introduction

Developing highly efficient visible light active photocatalysts is imperative for sustainable clean hydrogen production using renewable solar energy. The great challenges are generally the inferior charge carrier kinetics and the narrow visible light response, which lead to the unsatisfactory activities of most reported photocatalysts.[1] Constructing composites with aligned electronic structures and making use of the internal field has thus been widely explored to promote the transfer and separation of charge carriers in photocatalysis.[2] In this aspect, isotype

---

[a] *School of Metallurgy, Northeastern University, Shenyang 110819, Liaoning, P. R. China. E-mail: niup@smm.neu.edu.cn*

[b] *Department of Chemistry, College of Science, Northeastern University, Shenyang 110819, Liaoning, P. R. China*

[c] *Laboratory of Polymeric and Composite Materials (LPCM), Center of Innovation and Research in Materials and Polymers (CIRMAP), University of Mons (UMONS), Place du Parc 20, 7000 Mons, Belgium*

† Electronic supplementary information (ESI) available. See DOI: **https://doi.org/10.1039/d4ey00145a**

‡ Ping Niu, Haoqing Zhang and Jian Zeng contributed equally to this work.

heterojunctions constructed by monomers with similar components but different electronic structures, especially the ones synthesized *in situ* are endowed with great superiority due to the better-matched atomic structure of monomers and the optimized charge transfer by the intimate contact at the interface.[3] However, exploring isotype heterojunctions with wide and efficient visible light response for clean hydrogen production is still challenging due to the limited availability as well as intrinsic properties of monomers.

Polymeric carbon nitride with the merits of adjustable coordination environment and band structure, good physicochemical stability as well as high-cost effectiveness is a promising candidate as an ideal photocatalyst for various applications.[4,5] In the past decades, isotype heterojunctions of carbon nitride have been constructed generally by non-metal defects modifications of monomers.[6,7] However, carbon nitride obtained by direct polymerization of nitrogen-rich precursors generally has an incomplete condensed structure with plenty of undesirable detrimental defects, which leads to serious recombination of charge carriers and thus inferior photocatalytic activities. In recent years, ion-assisted reconstruction of carbon nitride (generally in molten alkali salts) with high crystallinity, high overall in-plane order and thus improved carrier transfer behaviors has aroused wide attention, including the poly(triazine imide) (PTI) and poly(heptazine imide) (PHI).[8–10] Comparatively, the strong visible absorption arising from the extended π-conjugated structure as well as the smooth charge carrier transfer makes poly(heptazine imide) (PHI) a promising candidate for solar energy conversion. Constructing the isotype heterojunctions of PHI is thus fascinating and may surpass the recently reported heterojunctions of PTI/PHI obtained by LiCl-involved eutectic salt calcination, considering the limited visible-light-response of PTI (intrinsic large bandgap of 2.92–3.2 eV).[11–16]

As reported, alkali ions (such as K^+ and Na^+) can embed into the skeletons of heptazine rings in the PHI structure considering the lone-pair electrons in the N-containing structures.[17] Interestingly, it is noticed that PHI evolved by different alkali ions (such as Na^+ and K^+) has distinctive phase characteristics, which is attributed to the different hydration properties of alkali ions,[18,19] and reflected in the distinctive layer stacking distance and the peak ratio of (100) and (002). However, as far as we know, there were no reports on the successful construction of different alkali ions-regulated isotype PHI heterojunctions. Considering the strong solvation effect of LiCl for the introduction of PTI,[20] and the structural defects introduction or framework destruction of PHI brought by the excessive reactivity of LiCl-involved molten salt,[21] it is indispensable for the exploration of non-molten/LiCl-free salt for the construction of high crystalline PHI isotype heterojunctions.[18,22,23] As reported, the calcination of precursors in typical binary NaCl/KCl salt with high melting point (m. p. = 652 °C) only results in the formation of 'Mel-PHI' with a low-ordered structure since the insufficient mass diffusion greatly restricts the complete crystalline growth.[20]

Considering the similar π-conjugated structures, graphite carbon rings can be incorporated in the in-plane framework of carbon nitride to modify the structure features (such as in-plane periodicity, stacking order, *etc.*) of carbon nitride,[24,25] and thus is assumed to influence the structure reconstruction of carbon nitride during salt-assisted calcination. Moreover, the incorporation of carbon rings has been reported to introduce the internal field and increase the diffusion length of charge carriers in carbon nitride by 10 times[24,25] to optimally regulate the electronic structure and promote effective charge transfer,[26–28] and thus is beneficial for higher photocatalytic efficiencies. In this work, by incorporating carbon rings in the framework of carbon nitride, the novel *in situ* growth of Na–PHI/K–PHI isotype heterojunction with high crystallinity of PHI monomers, intimate contact as well as carbon-related high-speed charge carrier transport channels is constructed for the first time, which is a significant innovation of the visible light responsive isotype heterojunctions. The carbon-decorated Na–PHI/K–PHI shows excellent charge carrier transfer kinetics as well as extended visible light absorption (up to 800 nm), which leads to superior photocatalytic hydrogen evolution activities under visible light irradiation.

2. Results and discussion

2.1. Carbon incorporation assisted structure evolution by theoretical simulation

As indicated in Fig. 1a, direct polymerization of melamine was applied for the synthesis of incompletely polymerized carbon nitride (melon). By comparison, through thermal copolymerization of glucose and melamine, carbon-incorporated melon (C-melon) can be obtained. Further treating C-melon and melon in the eutectic salt environment of NaCl/KCl eventually

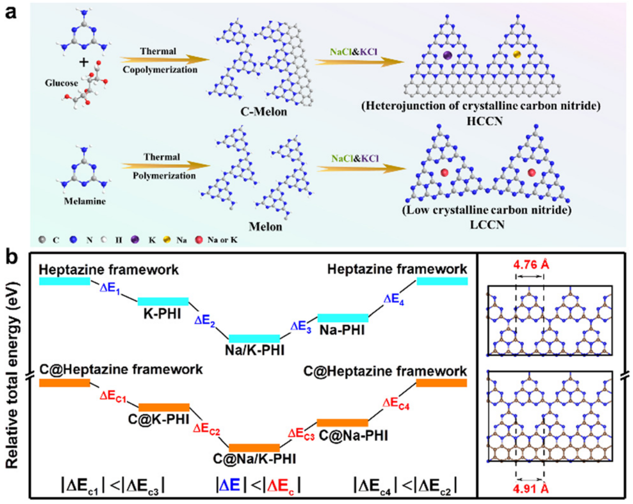

Fig. 1 (a) Schematic of the synthesis procedures as well as the distinctive structural evolution with and without carbon decoration. The grey, blue, purple and yellow spheres denote C, N, K and Na atoms. The magenta spheres denote random Na or K atom. (b) Theoretical illustration of the decreased formation energy and enlarged triangle hole size due to the carbon incorporation. ΔE_x and ΔE_{cx} represent the formation energy of alkali ion (Na or/and K) embedded heptazine framework with and without carbon rings, respectively.

results in the distinctive atomic structure of HCCN (heterojunction of crystalline carbon nitride) and LCCN (low crystalline carbon nitride), respectively. In other words, the incorporation of carbon rings has a significant influence on the structure evolution from melon to poly(heptazine imide) (PHI). In this aspect, the formation energy of different ion-embedded PHI (Na–PHI, K–PHI and Na/K–PHI) with or without carbon rings (structure models shown in Fig. S1, ESI†) was studied to reveal the possible structure evolution processes (Fig. 1b). According to the DFT calculation results (Table S1, ESI†), the formation energy in the presence of carbon rings is lower than that in the absence of carbon rings ($|\Delta E_{cx}| > |\Delta E_x|$), indicating the existence of carbon rings in the framework is beneficial for the embedding of ions. The existence of carbon rings can reduce the formation energy of Na/K–PHI obviously with the $|\Delta E|$ increasing from 3.06 to 3.30 eV (Table S2, ESI†). Moreover, the results show that $|\Delta E_{c3}| > |\Delta E_{c1}|$ and $|\Delta E_{c2}| > |\Delta E_{c4}|$ indicate Na$^+$ and K$^+$ would reinforce with each other in the embedding processes. Furthermore, the optimized structures show that the triangle holes in the heptazine framework expand from 4.76 Å to 4.91 Å when carbon rings are incorporated. Since the embedding of ions in the structure of carbon nitride is affected by the size of ion radius and the space limitations,[29,30] the enlarged size of holes may facilitate the embedding process more significantly. Therefore, it is concluded that the incorporation of carbon rings is favorable for the ion embedding processes, which can probably facilitate the ordered phase formation of Na–PHI/K–PHI.

2.2. Phase analysis and the structural verification of Na–PHI and K–PHI

Attributing to the π-conjugated structure characteristics, carbon-incorporated carbon nitride can form through polymerization of the in-plane connected triazine/carbon ring structure with sp^2-hybridized C–N bonds.[24] As shown in the XRD patterns (Fig. 2a), melon has typical diffraction peaks of semi/non-crystalline carbon nitride, with the peaks located at 13.2° and 27.7° corresponding to the periodic in-plane arrangement of NH/NH$_2$ bonded heptazine strands and the interlayer stacking, which can be referred to the (100) and (002) planes.[31] Compared with melon, the diffraction peak of C-melon shifted to lower angles with wider half-peak widths (Table S3, ESI†), indicating the carbon ring incorporation slightly expanded the local order of melon structure. As indicated in the FTIR spectra (Fig. S2, ESI†), C-melon basically maintained the functional groups of melon, including the typical vibration peaks of aromatic heptazine ring (810 cm^{-1}), aromatic C–N and C═N bonds (1200–1700 cm^{-1}), –NH$_2$/–NH and hydroxyl groups/water (3000–3500 cm^{-1}).[32–34] Interestingly, treating melon and C-melon under the same salt condition of NaCl/KCl results in distinctive phase structure evolution (Fig. 2b). For LCCN evolved from melon structure, the diffraction peak of (100) has shifted from 13.2° to 8.1°, confirming the formation of PHI structure.[14] Moreover, the LCCN has a broad diffraction peak of (002) located at around 27.8°, which indicates the roughly organized structure of LCCN with low crystallinity as well as chaotic ion dispersion due to the sluggish crystallize kinetics originating from the partial dissolution of carbon nitride in NaCl/KCl with high melting point.[20] In obvious contrast, HCCN (evolved from C-melon structure) shows well-developed facets with sharper diffraction patterns, indicating the significantly enhanced crystallinity and improved long order of the conjugated framework. In detail, the peaks located at 8.1°, 14.7°, 27.7°, 29.4°, 35.8° and 43.4° can be classified as (100), (110), (210), (002), (320) and (320) of Na–PHI, while the diffraction peaks at 28.5° and 38.6° can be identified as (002) and (171) of K–PHI.[16,23,35] Note that HCCN has clearly distinguishable twin peaks of (002) facets located at 27.7° and 28.5°, corresponding to the stacking spacing of 0.32 nm and 0.31 nm. The different stacking spacing can be assigned to the different embedding effects of ions in the framework of carbon nitride,[36] and the larger distance in Na–PHI originate from the slightly larger radius of hydrated Na$^+$ (3.6 Å) than hydrated K$^+$ (3.3 Å).[19]

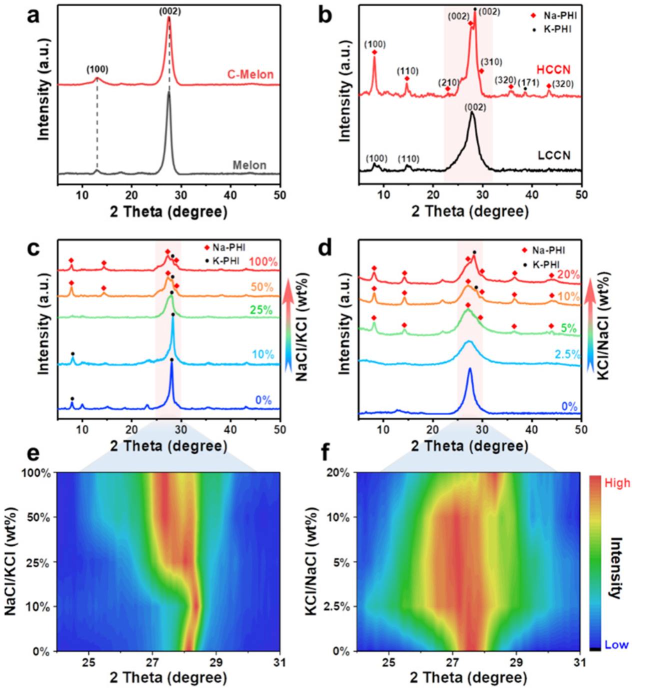

Fig. 2 XRD patterns of (a) melon and C-melon and (b) LCCN and HCCN. Samples obtained by calcinating C-melon in alkali salt environment with various ratio of (c) NaCl : KCl (0–100%) and (d) KCl : NaCl (0–20%). (e) and (f) Corresponding XRD contour plots of the local region indicated in (c) and (d), respectively.

To clarify the unique phase structure of HCCN from the commonly reported PHI/PTI heterojunctions and to reveal the structural evolution processes of Na–PHI/K–PHI, various salt environments, including LiCl, LiCl/KCl, and proportionally adjusted NaCl/KCl, were applied for the reconstruction of C-melon. As indicated, CN$_{\mathrm{LiCl}}$ has two dominant diffraction peaks of 26.4° and 29.3° (Fig. S3a, ESI†), which correspond to the (002) and (102) of PTI.[37] In addition, CN$_{\mathrm{LiCl/KCl}}$ synthesized in the LiCl/KCl salt shows the coexistence of PHI and PTI phases, with the diffraction peaks at 8.1° and 28.2° corresponding to the (100) and (002) of PHI and the diffraction peaks at 26.6° and

29.2° corresponding to the (002) and (102) of PTI (Fig. S3b, ESI†),[12,14] which is clearly different with HCCN obtained in this work. Furthermore, it is found that different compositions of NaCl/KCl salt can effectively regulate the phase structures. As shown in Fig. 2c, C-melon calcinated in singular KCl salt shows a sharp peak at 28.4° and a weak peak at 8.1°, corresponding to the (002) and (100) facets of K–PHI. Gradually increasing the amount of NaCl in KCl/NaCl salt, the diffraction peak at 28.4° shifts to lower angles. When the ratio of NaCl : KCl reaches 25%, the (002) diffraction obviously broadens compared with K–PHI, which is a reflection of the effective interaction between Na and K ions. Especially, with NaCl : KCl further increasing to 50%, the well-developed (100), (110), (002) and (310) facets corresponding to Na–PHI become distinguishable, and the relative content of Na–PHI increases with higher NaCl : KCl ratio (100%). A similar phase regulation effect was observed in the NaCl/KCl salts except that calcinating C-melon in singular NaCl salt did not result in the formation of Na–PHI (Fig. 2d) possibly due to the slow ion transfer kinetics originating from the high melting point of NaCl (m.p. = 801 °C) than KCl (m.p. = 770 °C). With the assistance of KCl, the formation of Na–PHI was promoted when the ratio of KCl : NaCl increased to 5%. Further increasing the ratio of KCl : NaCl results in the formation and enhancement of the K–PHI phase. The crystal phase distinction of Na–PHI and K–PHI was verified by the content of Na^+ and K^+ in Na–PHI and K–PHI. As indicated in Table S4 (ESI†), the K–PHI obtained in singular KCl salt shows the exclusive existence of K^+ (3.51%) while Na–PHI obtained in NaCl/KCl salt shows dominant existence of Na^+ (5.45%) with little existence of K^+ (0.88). The corresponding XRD contour plots in the range of 24–31° (Fig. 2e and f) gives intuitive presentation of the phase evolution processes under different NaCl/KCl environment, confirming the unique coexistence of Na–PHI and K–PHI in HCCN, which is different from all the currently reported phases in literature.[12,14,16]

It is worth mentioning that only with the appropriate amount of carbon decoration (0.1–0.5%) can the formation of Na–PHI/K–PHI be effectively induced. The phase structure of HCCN (0.2% glucose), low-C HCCN (0.1% glucose) and high-C HCCN (0.5% glucose) can be identified as the co-phase of Na–PHI/K–PHI (Fig. S4, ESI†). However, excessive glucose modification only leads to the formation of a low-ordered crystal structure similar to LCCN, as observed from the XRD patterns of LCCN-0.8% and LCCN-1% (Fig. S5, ESI†). It is interpreted that the inferior dispersion of glucose cannot effectively incorporate carbon rings in the carbon nitride skeleton and subsequently assist the growth of ordered PHI crystals. This assumption was further supported by the results that only phase structures similar to LCCN were obtained by calcinating the mixture of melon and graphitic carbon in NaCl/KCl (Fig. S6, ESI†).

2.3. Microstructure and atomic structure analysis

Compared with LCCN which shows thick bulk morphology with a large particle size of around 10 μm (Fig. S7, ESI†), HCCN presents lamellar morphology with smaller particle size (1–2 μm), which is confirmed by the SEM and TEM results (Fig. 3a and b). The lamellar morphology reflects the more sufficient template effect of NaCl/KCl and indicates the promoted crystal growth in the *z* direction in HCCN.[38] It is noted that HCCN has higher crystallinity than LCCN (Fig. 3c and Fig. S8, ESI†), which is consistent with the XRD results. The lattice fringes of 0.31 nm and 0.32 nm observed in HCCN indicate the development of two distinctive interlayer stacking (Fig. 3d and e), which corresponds to the (002) facets of K–PHI and Na–PHI and is consistent with the XRD results. Moreover, the lattice fringes of 0.22 nm are also observed in HCCN, indicating the existence of carbon units.[39] The HAADF images and their corresponding element mapping indicate the existence of C, N, Na and K both in LCCN and HCCN (Fig. 3f and Fig. S8, ESI†), which confirm the intercalation of alkali ions in the structure.

The incorporation of carbon rings in HCCN is evidenced by the higher atomic ratio of C : N from LCCN (0.68) to HCCN (0.71) as well as the Raman characterizations (Table S5 and Fig. 3g, ESI†). As indicated, HCCN showed obvious D and G peaks of carbon vibration at 1323 and 1565 cm^{-1}, respectively.[39] Higher content of glucose added leads to a higher degree of graphitization, as seen from the more obvious

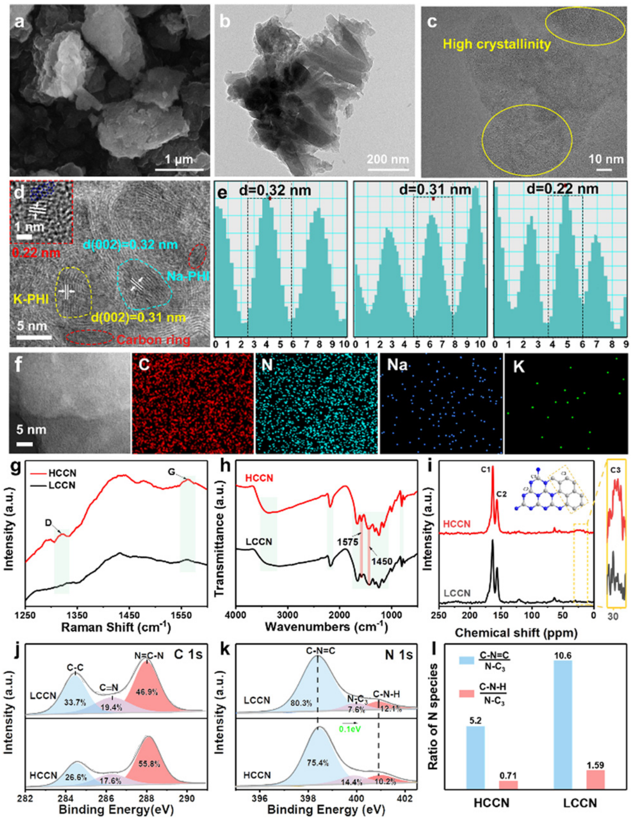

Fig. 3 (a) SEM, (b) and (c) TEM images of HCCN. (d) and (e) HRTEM image and the lattice fringes of HCCN. (f) HAADF image and the corresponding element distribution of HCCN. Structural characterizations for LCCN and HCCN. (g) Raman spectra, (h) FTIR spectra, (i) NMR spectra, deconvolution of (j) C 1s spectra and (k) N 1s spectra, (l) quantitative ratio of nitrogen species.

G-peak vibration in high C–HCCN (Fig. S9, ESI†). Note that LCCN shows weak peaks in the range of 500–1000 cm^{-1}, which originates from the vibration C–N═C linked heptazine units, indicating the relatively disordered structure of LCCN.[40,41] In contrast, low-C HCCN, HCCN and high-C HCCN all show strong vibration peaks in this range, representing the better-organized heptazine structures, which is consistent with the XRD results. The functional groups and chemical states of LCCN and HCCN show typical carbon nitride structure as revealed by the FTIR spectra (Fig. 3h). The peaks at 993 cm^{-1} and 1150 cm^{-1} originating from the symmetric and asymmetric vibration of NC2 in metal-NC2 groups confirm the embedding of alkali ions while the peak at 2180 cm^{-1} corresponds to the vibration modes of –C≡N groups.[9,17,18,23,33–35] Moreover, the enhanced peak around 3300 cm^{-1} indicates the probably better hydrophilicity of HCCN than LCCN, and the increased intensity of C═N signal at 1570 cm^{-1} for HCCN indicates the more complete heptazine framework (Fig. S10, ESI†). The new absorption peak appeared at 1450 cm^{-1} can be attributed to the carbon-induced reconstruction of the heptazine structure in HCCN.[42] The solid ^{13}C magic angle spinning nuclear magnetic resonance (MAS-NMR) spectroscopy further evidences the atomic structure. Both LCCN and HCCN show strong signals peaking at around 163 ppm and 156 ppm, which correspond to the [$CN_2(NH_x)$] (C1) and (CN_3) (C2) in the heptazine rings, respectively (Fig. 3i).[43] The decreased signal at 120 ppm arising from carbon atoms of the terminal NCN groups reflects the more compacted structure of HCCN.[36] Besides, the signals around 30 ppm probably arise from the structure of the carbon rings (C3) covalently connected to the heptazine rings in HCCN (the inset figure).

The XPS characterizations reveal the existence of C, N, O, Na, and K with no Cl for LCCN and HCCN (Fig. S11, ESI†), indicating the residual KCl and NaCl have been completely removed. The deconvolution of C 1s for LCCN and HCCN both have three peaks located at 284.5, 286.3 and 288 eV (Fig. 3j), corresponding to the bonding states of C═C/C–C (carbon impurities and structural carbon units), the edge C–NH_x and the aromatic N═C–N, respectively.[26,43] Comparatively, the decreased ratio of C–NH_x/N═C–N from 0.41 to 0.32 reflects the more complete structure of HCCN. The three deconvoluted peaks at 399.4, 399.9, and 400.9 eV in N 1s spectra for LCCN and HCCN indicate the existence of C–N═C (N_{2C}), bridging N–C_3 (N_{3C}), and amino C–N–H, respectively (Fig. 3k).[43] In contrast, the C–N═C and C–N–H in HCCN shifted toward higher binding energy by 0.1 eV, which possibly originates from the perturbation of electronic structure due to the incorporation of carbon rings in the heptazine framework. Furthermore, the quantitative analysis of nitrogen species shows a lower (C–N–H)/(N–C_3) value in HCCN (0.71) than that in LCCN (1.59) (Fig. 3l), and the less C–N–H content indicates the eliminated hydrogen bonds in HCCN, which further supports the more complete condensation in HCCN. Meanwhile, the (C–N═C)/(N–C_3) value decreases from 10.6 in LCCN to 5.2 in HCCN, indicating that HCCN has a more complete heptazine network.[44]

2.4. Optical properties and electronic structure analysis

The above results explicit the structure of LCCN and HCCN as low ordered PHI structure and carbon incorporated Na–PHI/K–PHI hetero-phase (C@Na–PHI/K–PHI), respectively, and the distinctive structure features result in significantly different electronic properties of LCCN and HCCN. As shown in the UV-Vis diffuse reflectance spectra (Fig. 4a), the light absorption edge slightly shifts from 467 nm for LCCN to 459 nm for HCCN and correspondingly the bandgap of HCCN increased by 0.05 eV compared with LCCN (Fig. S12, ESI†). The increased bandgap of HCCN can be possibly attributed to its unique framework, such as the higher long-order structure as well as the different stacking features.[20] Note that compared with literature reports, the larger deviated bandgap of K–PHI (2.72 eV) than Na–PHI (2.67 eV) possibly originated from the low crystallinity of Na–PHI obtained in this work (Fig. S13, ESI†), which further reveals the prominent crystallinity-related electronic structure characteristics of carbon nitride.[18,19] Except for the extended visible light absorption observed in carbon incorporated melon structure (Fig. S14, ESI†), HCCN has obviously extended visible light absorption in the wavelength longer than 500 nm compared with LCCN, which can be assigned to the incorporation effect of carbon rings in modifying the π-electron delocalization of carbon nitride.[25] The extension of visible light absorption makes it advantageous for HCCN to perform photocatalytic reactions under long wavelength visible light radiation.

The positive slope of the Mott–Schottky curves indicates the n-type semiconductor properties of HCCN and LCCN (Fig. S15, ESI†), which has been widely observed in carbon nitride materials.[12,45] Comparatively, the smaller slope of HCCN reveals the higher electron-donor density and mobility of

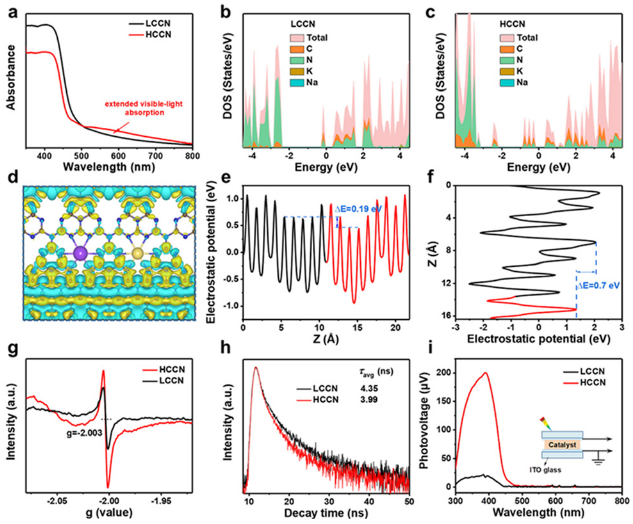

Fig. 4 (a) UV-Vis diffuse reflectance spectra. Calculated density of states for (b) LCCN and (c) HCCN. (d) Differential charge density between heptazine structure and carbon ring. Electrostatic potential profiles of (e) the interface of K–PHI and Na–PHI, and (f) the interface of PHI and carbon ring. (g) The electron spin resonance spectra, (h) Time resolved PL spectra and (i) SPV spectra of LCCN and HCCN.

charge carriers in HCCN than LCCN.[46] From the flat band potentials of LCCN (−1.0 V) and HCCN (−0.97 V) determined from the x-intercept values of the Mott–Schottky curves, the conduction band (CB) edges of LCCN and HCCN are calculated to be −0.9 and −0.87 V (*vs.* NHE), respectively.[47] Combined with the correspondingly calculated valence band (VB) edges, the band structure of LCCN and HCCN clearly indicates the more positive VB in HCCN and thus the stronger oxidation ability of holes, which is beneficial for the consumption of holes and thus the possibly decreased recombination of charge carriers. Similarly, the CB and VB edges of singular Na–PHI and K–PHI were obtained and the staggered alignment of the band structure indicates the probably built heterojunction as well as the internal electric field in HCCN (Fig. S16, ESI†), which can provide the strong driving force for the separation of charge carriers. To further reveal the electronic structure and charge transfer kinetics of LCCN and HCCN, DFT calculations based on the heptazine and heptazine/carbon integrated framework were carried out (Fig. S17, ESI†). The density of electron states (DOS) for LCCN and HCCN indicates the conduction and valence band is mainly composed of the C and N orbitals, respectively, and Na and K has little contribution to the band structure (Fig. 4b and c). Comparatively, the existence of carbon rings introduces multiple intermediate energy levels into the band gap of HCCN, which enhances the light absorption capacity of HCCN in the long wavelength range and agrees with the experimental results. Besides, it is found that there is strong charge coupling between heptazine and carbon ring in the covalent interface (Fig. 4d), and the charge distribution is delocalized, which would be beneficial for the separation of charge carriers.

Moreover, as seen from the curve of average self-consistent electrostatic potential for HCCN (Fig. 4e and f), the electrostatic potential of the carbon ring is significantly smaller than that of K/Na–PHI, forming a prominent potential drop in the x direction, which can effectively drive the photogenerated carrier migration. Similarly, the difference between K–PHI and Na–PHI also leads to a certain potential drop in the y direction and propels the charge transfer. It can be thus interpreted that the introduction of Na/K and carbon rings provides multi-directional built-in electric fields for HCCN and drives the charge separation and delocalization distribution, which can effectively inhibit the recombination of photogenerated charge carriers and enhance the photocatalytic activities.[14,48,49]

Experimentally, as observed in the room-temperature electron spin resonance (ESR) spectra (Fig. 4g), the Lorentz lines of both LCCN and HCCN have the g value of 2.003, due to the unpaired electrons originating from the π-conjugated heptazine units.[50] The increased ESR signal originating from the unpaired electrons on the carbon nitride units indicates the recombination of photoinduced charge has been effectively prohibited, which proves the significantly modified charge carrier behaviors.[51] Besides, the higher photocurrent of HCCN (around 7 times that of LCCN) and the smaller radius of a semicircle in EIS Nyquist plot indicates the superior transfer/separation rate and efficiency of charge carriers in HCCN (Fig. S18a and b, ESI†).[52] The superior charge carrier transfer kinetics in HCCN is also confirmed by the PL characterizations. The obviously lower photoluminescence intensity of HCCN in the steady state PL spectra indicates the effectively suppressed recombination of photogenerated charge carriers, while the slightly blue-shifted photoluminescence peak from 482 nm (LCCN) to 466 nm (HCCN) agrees with the slightly larger bandgap of HCCN (Fig. S18c, ESI†). The time-resolved fluorescence decay spectra reveal the decreased lifetime of charge carriers for HCCN (Fig. 4h), indicating more photogenerated electron–hole pairs can be separated and the exciton recombination is suppressed.[53,54] Furthermore, the surface photovoltage (SPV) measurement was further applied to identify the transfer and separation behaviors of charge carriers. For n-type semiconductors, the photogenerated holes would transfer to the surface under light irradiation, leading to the positive SPV responses.[6,55] Note that the LCCN shows rather weak signal (values smaller than 25 μV), indicating the sluggish transfer of charge carriers (Fig. 4i). However, the HCCN shows obviously much stronger signal (maximum value around 200 μV), reflecting the strong extracting ability of holes to the surface in HCCN, which can be ascribed to the heterojunction effect between the monomers (C/Na–PHI/K–PHI). These results effectively support the advantageous charge carrier separation efficiency in HCCN.

2.5. Photocatalytic hydrogen evolution activities under visible light irradiation

To acknowledge the performances of various materials, photocatalytic hydrogen evolution activities were evaluated by applying triethanolamine as the sacrificial agent to consume holes. First of all, C-melon shows a much higher hydrogen evolution rate than that of melon due to the effective carbon modification (Fig. S19, ESI†). Despite this, both melon (11 μmol g^{-1} h^{-1}) and C-melon (65 μmol g^{-1} h^{-1}) still have inferior hydrogen evolution activities, ascribing to the incomplete condensed structure of melon. In contrast, LCCN, HCCN, Na–PHI and K–PHI have increased activities by order of magnitude under visible light irradiation (Fig. 5a), which supports the significance of salt-assisted structure reconstruction.[9,41] Comparatively, the hydrogen evolution rate of HCCN is as high as 3609 μmol g^{-1} h^{-1}, which is around 5.7, 6.8 and 4.5 times that for LCCN (636 μmol g^{-1} h^{-1}), Na–PHI (533 μmol g^{-1} h^{-1}) and K–PHI (803 μmol g^{-1} h^{-1}) respectively (Fig. 5b), indicating the superiority of HCCN. As indicated in Fig. 5c, HCCN exhibits continuous and stable hydrogen evolution performance without obvious activity decay during the 3-cycle tests (lasting for 9 h) and the slight decrease in the fourth cycle can be attributed to the consumption of sacrificial agent.[16] For further stability analysis, the elemental proportion as well as structure characterizations of HCCN before and after the photocatalytic hydrogen evolution reaction were performed. As indicated by the XRD patterns (Fig. S20, ESI†) and the EA results (Table S6, ESI†), the phase structure as well as the elemental proportion of HCCN was largely retained after the reaction, which further reveals the high cycling stability of HCCN. Note the newly

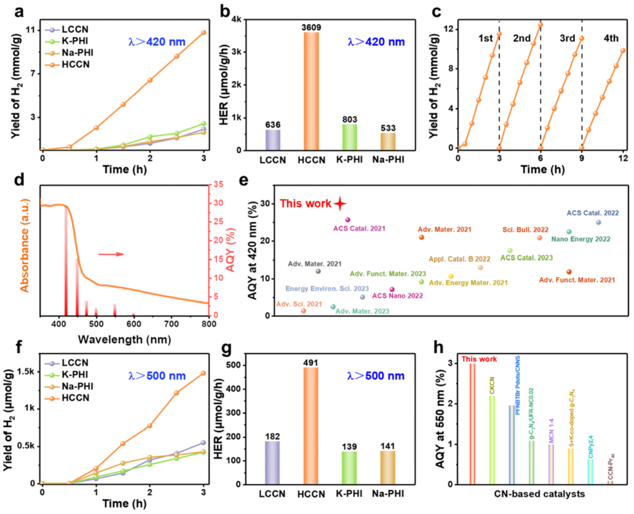

Fig. 5 (a) Time dependent hydrogen evolution courses and (b) hydrogen evolution rates of LCCN, HCCN, Na–PHI and K–PHI under the irradiation of λ > 420 nm. (c) Cycling stability of HCCN under the irradiation of λ > 420 nm. (d) Wavelength dependent hydrogen evolution AQY values together with the light absorption properties of HCCN. (e) AQY comparation of HCCN with literatures (λ = 420 nm). (f) Time dependent hydrogen evolution courses and (g) hydrogen evolution rates of LCCN, HCCN, Na–PHI and K–PHI under the irradiation of λ > 500 nm. (h) AQY value comparation of HCCN with the reported values in literatures (λ = 550 nm).

appeared diffraction peaks at 39° and 46° assigning to the (111) and (002) crystal planes of Pt indicate the successful photodeposition of Pt cocatalysts on HCCN.[56]

The apparent quantum yield (AQY) trend is highly consistent with the light absorption properties of HCCN (Fig. 5d and Table S7, ESI†), indicating the hydrogen evolution originates from photocatalysis processes. Especially, the AQY of HCCN reaches 29.3% at 420 nm, which exceeds most of the reported values (Fig. 5e and Table S8, ESI†). The superior photocatalytic hydrogen evolution activity of HCCN is closely related to the significantly modified charge carrier behaviors, especially the promoted transfer/separation kinetics attributing to the successful carbon incorporation as well as the isotype heterojunction effect of Na–PHI/K–PHI. It is noticed that the high-C HCCN has lower hydrogen evolution activity (3014 μmol g^{-1} h^{-1}) than HCCN (Fig. S21, ESI†), which is probably due to the increased content of the low active Na–PHI phase. Furthermore, under long wavelength light irradiation (Fig. 5f, g and Fig. S22, ESI†), the hydrogen evolution rate of HCCN is up to 491 μmol g^{-1} h^{-1} even under the irradiation of λ > 500 nm, which is around 2.7, 3.5 and 3.5 times that of LCCN (182 μmol g^{-1} h^{-1}), Na–PHI (139 μmol g^{-1} h^{-1}) and K–PHI (141 μmol g^{-1} h^{-1}), respectively. The AQY of HCCN under λ = 550 nm (3%) exceeds the majority of the reported photocatalysts (Fig. 5h and Table S9, ESI†). Especially, note that even under the irradiation of λ = 600 nm, the HCCN still shows a hydrogen evolution rate around 5 times that of LCCN (Fig. S23, ESI†), further indicating the superior structure advantage of HCCN in long wavelength light-driven photocatalysis. Interestingly, the high-C HCCN shows the highest hydrogen evolution rate under the irradiation of λ > 500 nm (Fig. S22, ESI†) and λ = 600 nm, attributed to its stronger visible light absorption under wavelength longer than 500 nm (Fig. S24, ESI†).

3. Conclusions

In this work, the incorporation of carbon rings into the melon framework reduces the formation energy, enabling successful growth of a novel isotype heterojunction of PHI with high crystallinity. The formation of PHI, the hetero-phase junction between Na–PHI and K–PHI, as well as the existence of carbon rings contributes to the smooth transfer and separation kinetics of charge carriers. Moreover, the visible light absorption has been extended up to 800 nm due to the carbon-induced intermediate levels in the bandgap. The synthesized HCCN has superior hydrogen evolution activities under the irradiation of λ > 420 nm (3609 μmol g^{-1} h^{-1}) as well as under long wavelength light irradiation (λ = 600 nm). This work may inspire extensive attempts for the design and construction of novel heterojunctions as well as the design of highly efficient visible light photocatalysts.

Author contributions

Ping Niu: conceptualization, investigation, resources, funding acquisition, writing – original draft. Haoqing Zhang: data curation, formal analysis, methodology. Jian Zeng: data curation, investigation, software. Tianjian Hu: investigation, validation. Meixue Zhang: investigation, validation. Chengyao Xie: investigation, validation. Jérémy Odent: investigation, validation. Boyin Zhai: formal analysis. Shulan Wang: resources. Li Li: supervision, funding acquisition, writing – review & editing.

Data availability

The authors confirm that the data supporting the findings of this study are available within the article and its ESI.†

Conflicts of interest

There are no conflicts to declare.

Acknowledgements

This work was supported by the National Natural Science Foundation of China (52372179, 51902045, 22378055), Applied Basic Research Program of Liaoning (2022JH2/101300200), Liaoning International Science and Technology Cooperation plan 2023JH2/10700021, Guangdong Basic and Applied Basic Research Foundation (2022A1515140188), Fundamental Research Funds for the Central Universities (N2225038, N2002005, N2125004, N2225044), and Young Elite Scientist Sponsorship Program by CAST (YESS) 2019-2021QNRC. We also appreciate the instrumental analysis from Analytical and Testing Center, Northeastern University.

References

1 P. Zhou, I. A. Navid, Y. Ma, Y. Xiao, P. Wang, Z. Ye, B. Zhou, K. Sun and Z. Mi, *Nature*, 2023, **613**, 66–70.
2 J. Wang, Y. Zhang, S. Jiang, C. Sun and S. Song, *Angew. Chem., Int. Ed.*, 2023, e202307808.
3 X. Wang, Q. Xu, M. Li, S. Shen, X. Wang, Y. Wang, Z. Feng, J. Shi, H. Han and C. Li, *Angew. Chem., Int. Ed.*, 2012, **51**, 13089–13092.
4 G. Liao, Y. Gong, L. Zhang, H. Gao, G.-J. Yang and B. Fang, *Energy Environ. Sci.*, 2019, **12**, 2080–2147.
5 P. Niu, J. Dai, X. Zhi, Z. Xia, S. Wang and L. Li, *InfoMat*, 2021, **3**, 931–961.
6 D. Zhao, Y. Wang, C.-L. Dong, Y.-C. Huang, J. Chen, F. Xue, S. Shen and L. Guo, *Nat. Energy*, 2021, **6**, 388–397.
7 J. Zhang, M. Zhang, R.-Q. Sun and X. Wang, *Angew. Chem., Int. Ed.*, 2012, **51**, 10145–10149.
8 L. Lin, Z. Yu and X. Wang, *Angew. Chem., Int. Ed.*, 2019, **131**, 6225–6236.
9 G. Zhang, J. Zhu, Y. Xu, C. Yang, C. He, P. Zhang, Y. Li, X. Ren and H. Mi, *ACS Catal.*, 2022, **12**, 4648–4658.
10 H. Zhang, Z. Xia, P. Niu, X. Zhi, R. Dai, S. Chen, S. Wang and L. Li, *Catal. Sci. Technol.*, 2022, **12**, 5372–5378.
11 F. Li, X. Yue, Y. Liao, L. Qiao, K. Lv and Q. Xiang, *Nat. Commun.*, 2023, **14**, 3901.
12 Y. Li, F. Gong, Q. Zhou, X. Feng, J. Fan and Q. Xiang, *Appl. Catal., B*, 2020, **268**, 118381.
13 L. Lin, C. Wang, W. Ren, H. Ou, Y. Zhang and X. Wang, *Chem. Sci.*, 2017, **8**, 5506–5511.
14 J. Zhang, X. Liang, C. Zhang, L. Lin, W. Xing, Z. Yu, G. Zhang and X. Wang, *Angew. Chem., Int. Ed.*, 2022, **61**, e2022108.
15 L. Lin, Z. Lin, J. Zhang, X. Cai, W. Lin, Z. Yu and X. Wang, *Nat. Catal.*, 2020, **3**, 649–655.
16 S. Shen, J. Chen, Y. Wang, C.-L. Dong, F. Meng, Q. Zhang, Y. Huangfu, Z. Lin, Y.-C. Huang, Y. Li, M. Li and L. Gu, *Sci. Bull.*, 2022, **67**, 520–528.
17 G. Liu, Z. Tang, X. Gu, N. Li, H. Lv, Y. Huang, Y. Zeng, M. Yuan, Q. Meng, Y. Zhou and C. Wang, *Appl. Catal., B*, 2022, **317**, 121752.
18 Z. Chen, A. Savateev, S. Pronkin, V. Papaefthimiou, C. Wolff, M. G. Willinger, E. Willinger, D. Neher, M. Antonietti and D. Dontsova, *Adv. Mater.*, 2017, **29**, 1700555.
19 J. Kroger, F. Podjaski, G. Savasci, I. Moudrakovski, A. Jimenez-Solano, M. W. Terban, S. Bette, V. Duppel, M. Joos, A. Senocrate, R. Dinnebier, C. Ochsenfeld and B. V. Lotsch, *Adv. Mater.*, 2022, **34**, e2107061.
20 G. Zhang, L. Lin, G. Li, Y. Zhang, A. Savateev, S. Zafeiratos, X. Wang and M. Antonietti, *Angew. Chem., Int. Ed.*, 2018, **57**, 9372–9376.
21 F. K. Kessler and W. Schnick, *Z. Anorg. Allg. Chem.*, 2019, **645**, 857–862.
22 G. Zhang, G. Li, T. Heil, S. Zafeiratos, A. Savateev, X. Wang and M. Antonietti, *Angew. Chem., Int. Ed.*, 2019, **58**, 3433–3437.
23 F. Guo, B. Hu, C. Yang, J. Zhang, Y. Hou and X. Wang, *Adv. Mater.*, 2021, **33**, e2101466.
24 W. Che, W. Cheng, T. Yao, F. Tang, W. Liu, H. Su, Y. Huang, Q. Liu, J. Liu, F. Hu, Z. Pan, Z. Sun and S. Wei, *J. Am. Chem. Soc.*, 2017, **139**, 3021–3026.
25 L. Jian, H. Zhao, Y. Dong, J. Xu, Q. Mao, R. Ji, Z. Yan, C. Pan, G. Wang and Y. Zhu, *Catal. Sci. Technol.*, 2022, **12**, 7379–7388.
26 G. Jia, Y. Wang, X. Cui, Z. Yang, L. Liu, H. Zhang, Q. Wu, L. Zheng and W. Zheng, *Appl. Catal., B*, 2019, **258**, 117959.
27 J. Liu, Y. Yu, R. Qi, C. Cao, X. Liu, Y. Zheng and W. Song, *Appl. Catal., B*, 2019, **244**, 459–464.
28 M. Uzzaman, M. H. Suhag, H. Katsumata, I. Tateishi, M. Furukawa and S. Kaneco, *Catal. Sci. Technol.*, 2024, **14**, 267–278.
29 T. Xiong, W. Cen, Y. Zhang and F. Dong, *ACS Catal.*, 2016, **6**, 2462–2472.
30 W. Wang, H. Zhang, S. Zhang, Y. Liu, G. Wang, C. Sun and H. Zhao, *Angew. Chem., Int. Ed.*, 2019, **58**, 16644–16650.
31 B. V. Lotsch, M. Doblinger, J. Sehnert, L. Seyfarth, J. Senker, O. Oeckler and W. Schnick, *Chem. Eur. J.*, 2007, **13**, 4969–4980.
32 X. Zhi, H. Liu, Z. Xia, S. Di, Y. Beom Cho, P. Niu, S.-E. Chun, S. Wang and L. Li, *Solar RRl*, 2022, **6**, 2100901.
33 J. Kröger, A. Jiménez-Solano, G. Savasci, P. Rovó, I. Moudrakovski, K. Küster, H. Schlomberg, H. A. Vignolo-González, V. Duppel, L. Grunenberg, C. B. Dayan, M. Sitti, F. Podjaski, C. Ochsenfeld and B. V. Lotsch, *Adv. Energy Mater.*, 2020, **11**, 2003016.
34 X. Zhang, J. Yan and L. Y. S. Lee, *Appl. Catal., B*, 2021, **283**, 119624.
35 Y. Xu, X. He, H. Zhong, D. J. Singh, L. Zhang and R. Wang, *Appl. Catal., B*, 2019, **246**, 349–355.
36 H. Schlomberg, J. Kroger, G. Savasci, M. W. Terban, S. Bette, I. Moudrakovski, V. Duppel, F. Podjaski, R. Siegel, J. Senker, R. E. Dinnebier, C. Ochsenfeld and B. V. Lotsch, *Chem. Mater.*, 2019, **31**, 7478–7486.
37 J. Yang, Y. Liang, K. Li, G. Yang, K. Wang, R. Xu and X. Xie, *Appl. Catal., B*, 2020, **262**, 118252.
38 N. Díez, A. B. Fuertes and M. Sevilla, *Energy Storage Mater.*, 2021, **38**, 50–69.
39 X. Fang, R. Gao, Y. Yang and D. Yan, *Iscience*, 2019, **16**, 22–30.
40 L. Chen, D. Zhu, J. Li, X. Wang, J. Zhu, P. S. Francis and Y. Zheng, *Appl. Catal., B*, 2020, **273**, 119050.
41 L. Lin, H. Ou, Y. Zhang and X. Wang, *ACS Catal.*, 2016, **6**, 3921–3931.
42 Z. Pan, M. Liu, G. Zhang, H. Zhuzhang and X. Wang, *J. Phys. Chem. C*, 2021, **125**, 9818–9826.
43 F. Yang, D. Liu, Y. Li, L. Cheng and J. Ye, *Appl. Catal., B*, 2019, **240**, 64–71.
44 S. An, G. Zhang, K. Li, Z. Huang, X. Wang, Y. Guo, J. Hou, C. Song and X. Guo, *Adv. Mater.*, 2021, **33**, e2104361.
45 B. Zhai, H. Li, G. Gao, Y. Wang, P. Niu, S. Wang and L. Li, *Adv. Funct. Mater.*, 2022, **32**, 2207375.
46 F. Wei, Y. Liu, H. Zhao, X. Ren, J. Liu, T. Hasan, L. Chen, Y. Li and B. L. Su, *Nanoscale*, 2018, **10**, 4515–4522.
47 Y. Lin, W. Su, X. Wang, X. Fu and X. Wang, *Angew. Chem., Int. Ed.*, 2020, **59**, 20919–20923.

48 H. Ming, P. Zhang, Y. Yang, Y. Zou, C. Yang, Y. Hou, K. Ding, J. Zhang and X. Wang, *Appl. Catal., B*, 2022, **311**, 121341.

49 Z. Ma, X. Zong, Q. Hong, L. Niu, T. Yang, W. Jiang, D. Qu, L. An, X. Wang, Z. Kang and Z. Sun, *Appl. Catal., B*, 2022, **319**, 121922.

50 J. Chen, C. L. Dong, D. Zhao, Y. C. Huang, X. Wang, L. Samad, L. Dang, M. Shearer, S. Shen and L. Guo, *Adv. Mater.*, 2017, **29**, 1606198.

51 J. Zhang, Y. Li, X. Zhao, H. Zhang, L. Wang, H. Chen, S. Wang, X. Xu, L. Shi, L.-C. Zhang, J.-P. Veder, S. Zhao, G. Nealon, M. Wu, S. Wang and H. Sun, *ACS Nano*, 2020, **14**, 17505–17514.

52 B. Li, W. Peng, J. Zhang, J. C. Lian, T. Huang, N. Cheng, Z. Luo, W. Q. Huang, W. Hu, A. Pan, L. Jiang and G. F. Huang, *Adv. Funct. Mater.*, 2021, **31**, 2100816.

53 H. Che, X. Gao, J. Chen, J. Hou, Y. Ao and P. Wang, *Angew. Chem., Int. Ed.*, 2021, **60**, 25546–25550.

54 C. Cheng, J. Zhang, B. Zhu, G. Liang, L. Zhang and J. Yu, *Angew. Chem., Int. Ed.*, 2023, **62**, e202218688.

55 Y. Y. Kang, H. Z. Qi, G. D. Wan, C. Zhen, X. X. Xu, L. C. Yin, L. Z. Wang, G. Liu and H. M. Cheng, *Joule*, 2022, **6**, 1876–1886.

56 J. Wu, X. Xi, W. Zhu, Z. Yang, P. An, Y. Wang, Y. Li, Y. Zhu, W. Yao and G. Jiang, *Chem. Eng. J.*, 2022, **442**, 136334.